nature geoscience

Article

https://doi.org/10.1038/s41561-023-01372-3

Stress-driven recurrence and precursory moment-rate surge in caldera collapse earthquakes

Received: 7 August 2023

Accepted: 21 December 2023

Published online: 05 February 2024

Check for updates

Paul Segall[1] ✉, Mark V. Matthews[2], David R. Shelly[3], Taiyi A. Wang[1] & Kyle R. Anderson[4]

Predicting the recurrence times of earthquakes and understanding the physical processes that immediately precede them are two outstanding problems in seismology. Although geodetic measurements record elastic strain accumulation, most faults have recurrence intervals longer than available measurements. Foreshocks provide the principal observations of processes before mainshocks, but variability between sequences limits generalizations of pre-failure behaviour. Here we analyse seismicity and deformation data for highly characteristic caldera collapse earthquakes from 2018 Kīlauea Volcano (Hawaii, USA), with a mean recurrence interval of 1.4 days. These events provide a unique test of stress-induced earthquake recurrence and document processes preceding mainshocks with magnitude greater than five. We show that recurrence intervals are well predicted by stress histories inferred from near-field deformation measurements and that cycle-averaged seismicity reveals a critical phase, minutes before mainshocks, where earthquakes grew larger and seismic moment rate surged dramatically. The average moment rate in the final 15 minutes (0.7% of the mean cycle duration) was 4.75 times the background, a highly significant change. We infer that as the average stress increased, ruptures were more likely to overcome geometric barriers and grow larger, leading to characteristic, whole-fault ruptures. These findings imply that stress heterogeneity influences both earthquake nucleation and growth, including on potentially hazardous tectonic faults.

Earthquakes occur when accumulating shear stresses reach a fault's frictional strength[1,2]. Quantitative application to recurrence estimation has been challenging because (1) characteristic ruptures[3] are rare, (2) recurrence intervals are typically centuries or longer (for example, the San Andreas Fault[4] and the moment magnitude M_W 9 Tohoku-oki megathrust earthquake[5]), (3) geodetic observations typically span only a fraction of the earthquake cycle, making it challenging to infer strain/stress accumulation, and (4) long recurrence intervals allow other factors, including stress perturbations from nearby ruptures, to influence cycle duration.

Foreshocks provide principal observations of processes in focal regions before mainshocks. Seismicity rates[6,7] and the relative frequency of larger events[8,9] may increase before mainshocks. Earthquakes typically follow the Gutenberg–Richter (GR) size distribution, $N \propto 10^{-bM}$, where N is the frequency of events of magnitude M or larger and b is a constant of order unity. A decrease in b, representing

[1]Geophysics Department, Stanford University, Stanford, CA, USA. [2]Walden Consulting, Pittsfield, MA, USA. [3]Geologic Hazards Science Center, US Geological Survey, Golden, CO, USA. [4]Volcano Science Center, US Geological Survey, Moffett Field, CA, USA. ✉e-mail: segall@stanford.edu

https://doi.org/10.1038/s41561-023-01372-3

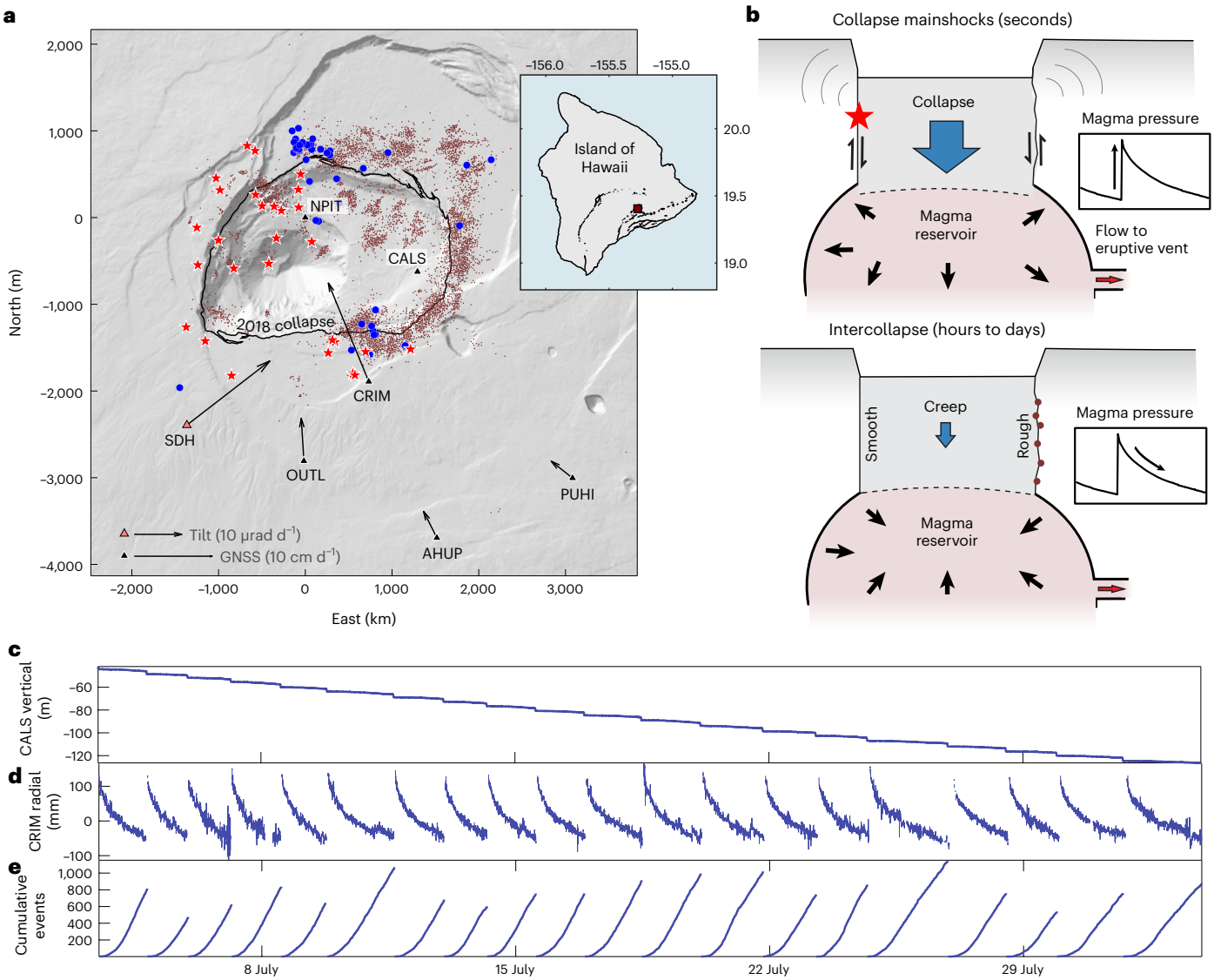

Fig. 1 | Summary of observations. a, Map showing GNSS (four-letter codes) and tilt stations (three-letter codes) with average inter-collapse displacement and tilt rates. Earthquake epicentres are shown for $M > 5$ mainshock events (red stars), the 50 largest VT events, $3.7 < M < 4.4$ events (blue) and smaller VT events (small red dots). **b**, Cross-section showing cycles with collapse mainshocks pressurizing the magma chamber, with magma outflow during the inter-collapse period leading to pressure decrease. **c**–**e**, Time series for the last 19 collapse cycles at Kīlauea in 2018. **c**, Vertical displacement (metres) of the GNSS station CALS. **d**, Radial displacement of the GNSS station CRIM (millimetres). **e**, Cumulative number of VT earthquakes per cycle. Earthquake locations from ref. 27. For the three VLP/mainshocks not relocated by ref. 27, we plot the HVO epicentres. Panel **b** adapted from ref. 19, Annual Reviews.

a greater fraction of large events, has been observed in laboratory experiments[10]. Dynamic rupture simulations on geometrically rough faults have shown that the probability of large events increases with increasing loading stress[11]. Ref. 12 reported *b*-value variation with tectonic environment and, by implication, stress; however, the specific stress dependence and the implication for foreshock behaviour is poorly constrained in situ.

Understanding mainshock recurrence and precursors would be advanced by a well-recorded sequence of characteristic earthquakes, which could be used to test recurrence models and average foreshock behaviour over multiple cycles. Dozens of repeating $M > 5$ caldera collapse earthquakes at Kīlauea Volcano, Hawaii, in 2018[13] provide such a dataset. These characteristic earthquakes[14] ruptured the same ring fault system (that is, are full-fault ruptures) with a mean recurrence interval of less than 1.5 days, a factor of ~7,000 times shorter than the characteristic Parkfield, California earthquakes on the San Andreas Fault[15]. A dense geodetic network measured inter-collapse deformation[16] that constrains the ring fault stressing history. The short repeat times and high stressing rates (megapascals (MPa) per day rather than megapascals per century) minimized the influence of stress transfer from neighbouring faults.

Volcanic collapse earthquakes are distinct from tectonic earthquakes in being depleted in high-frequency shaking due to interaction of the caldera block with the underlying magma reservoir[17]. The frequency content of the mainshocks does not, however, impact either their recurrence times or pre-mainshock behaviour.

The 2018 caldera collapse events

Between May and August of 2018, Kīlauea Volcano erupted more than 1 km^3 of basalt[18], causing the summit to collapse in 62 discrete events. During each of the final ~50 events, the caldera floor dropped several metres into the magma reservoir[13] in less than 10 s (ref. 19), generating $M > 5$ very-long-period (VLP) earthquakes (Fig. 1). Between these collapses, the Global Navigation Satellite System (GNSS) stations CALS

https://doi.org/10.1038/s41561-023-01372-3

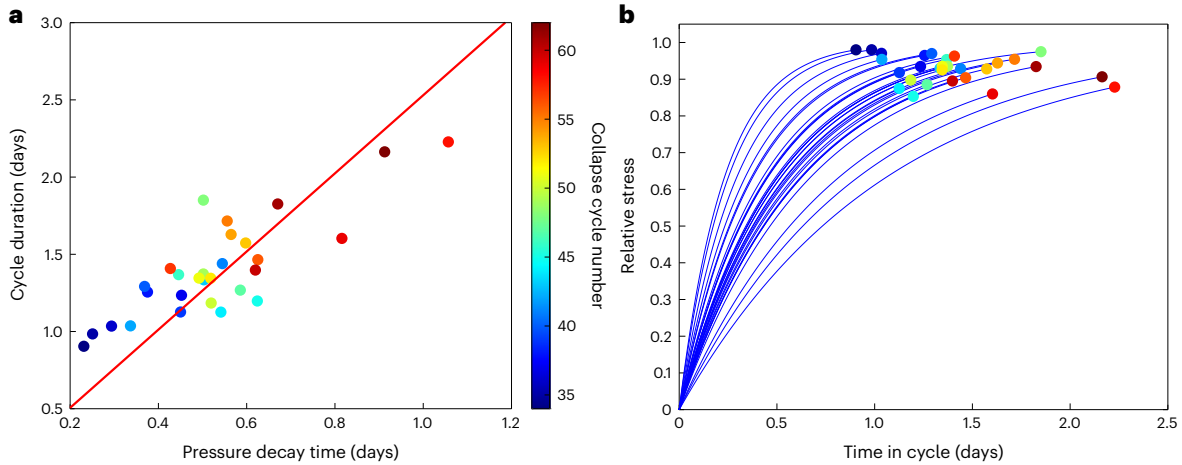

Fig. 2 | Test of inter-event recurrence times. a, Recurrence time versus pressure decay time t_c for the last 29 cycles. The colour scale refers to the collapse cycle number (62 events in total). The red line is the linear fit. **b**, Relative stressing histories $(\tau(t) - \tau_0)/\mathcal{T}$ for the last 29 cycles based on measured t_c. Dots indicate cycle end; colours show cycle numbers as in **a**.

and NPIT on the down-dropped block (Fig. 1c) subsided by several metres, indicating extensive ring fault creep[20]. Caldera formation was accompanied by thousands of volcano-tectonic (VT) earthquakes. VT activity ceased immediately following collapse mainshocks and then built up to nearly constant rates of hundreds of events per day (Fig. 1e)[21,22]. Multiple lines of evidence, including the strong correlation between cumulative VT seismicity and CALS displacement, indicate that most, but not all, VT earthquakes were caused by failure of asperities driven by ring fault creep[20].

Extra-caldera GNSS stations exhibited 'inflationary' deformation (radially outwards and up) during collapses due to pressurization of the underlying magma chamber and exponentially decaying 'deflation' (inwards and down) between collapses (Fig. 1d) from the outflow of magma and pressure decrease within the sub-caldera magma chamber[23,24].

A new fault segment propagated across the old caldera floor in June 2018, linking pre-existing faults along the north, west and south sectors to form a roughly circular ring fault[13]. Most VT seismicity was associated with this new eastern segment (Fig. 1a). Here we focus on the final 29 caldera collapse mainshocks beginning on 24 June 2018, after the ring fault was fully formed, although our results did not change materially by including additional cycles. During this period, mainshock recurrence times ranged from 0.90 to 2.2 days, with a mean of 1.4 days and a coefficient of variation of 0.23.

Controls on earthquake recurrence

Seismic slip occurred when shear stress on the ring fault reached the static frictional resistance. We employed extra-caldera GNSS and tilt data to estimate the temporal change in spatially averaged ring fault shear stress (Methods). The exponential decay of co-collapse inflation between collapses (Fig. 1b) was consistent with the flow of magma from the chamber to the eruption site, with a time constant t_c of ~0.5 days[24], although there was considerable inter-cycle variability[16]. Modelling geodetic and seismic data showed 2–3 MPa pressure increases during collapse earthquakes[16,17,25].

Between collapses, the weight of the caldera block(s) was balanced by magma pressure at its base and vertical shear stress τ on its sides[26]. With exponential decay in chamber pressure, the spatially averaged vertical shear stress on the ring fault increased as

$$\tau(t) = \mathcal{T}[1 - e^{-t/t_c}] + \tau_0 \quad (1)$$

where τ_0 is the initial shear stress and $\mathcal{T}$ is the stress-change scale (Methods). The co-collapse stress drop $\Delta\tau = \tau(T) - \tau_0$, where T is the cycle duration, is in the order of 1 MPa (ref. 17).

For a given $\mathcal{T}$, the pressure decay time t_c controls how rapidly stress accumulates. From equation (1), we expect the recurrence time T to scale as $T = -t_c \log[1 - (\tau(T) - \tau_0)/\mathcal{T}]$. Figure 2a confirms that faster decay in inflationary displacement correlates with shorter recurrence intervals. This correlation is highly significant ($r = 0.83$), with a root mean square prediction error of 0.26 days, equivalent to 19% of the mean cycle duration. This convincingly verified that the average stressing rate controlled earthquake recurrence. Deviations from the simple prediction could arise due to variations in $\mathcal{T}$ and τ_0 between cycles. However, these are difficult to estimate, as are possible changes in normal stress. Models with a free intercept or higher order nonlinear terms improve fit, but we defer such extensions until physical foundations are clear. Figure 2b shows the relative stressing histories $(\tau(t) - \tau_0)/\mathcal{T}$ with observed cycle durations. Due to heterogeneity, we do not necessarily expect a constant failure threshold, as discussed below.

Foreshock rates and magnitudes

We utilized the catalogue of ref. 27, which detected smaller earthquakes with template matching[28] and located hypocentres with waveform cross-correlation-derived relative travel times. This catalogue is statistically complete for magnitudes $M > 2.4$. We found that magnitude biases in the United States Geological Survey (USGS)/Hawaiian Volcano Observatory (HVO) catalogue distort the size distribution for $M \leq 3.3$ events (Supplementary Fig. 1). Nonetheless, key observations here are confirmed with the USGS catalogue (Supplementary Fig. 2).

Collapse mainshocks lack decaying aftershock sequences[22,29]. We suggest that this occurs because, rather than transferring stress to the neighbouring crust as in tectonic earthquakes, collapses are nearly rigid body motions[25] that relax accumulated stresses. Seismicity following mainshocks built up to quasi-steady rates well before subsequent events (Fig. 1e). The rapid seismicity onset following quiescence implies that ring fault stresses are highly heterogeneous, locally reaching failure at low average stress. The concentration of seismicity around the new (eastern) fault sector (Fig. 1a) suggests that fault roughness generates stress heterogeneity[30], although aseismic creep[20] also plays a role.

The long-period character of collapse mainshocks results from the dynamics of caldera collapse into the underlying magma chamber[17],

https://doi.org/10.1038/s41561-023-01372-3

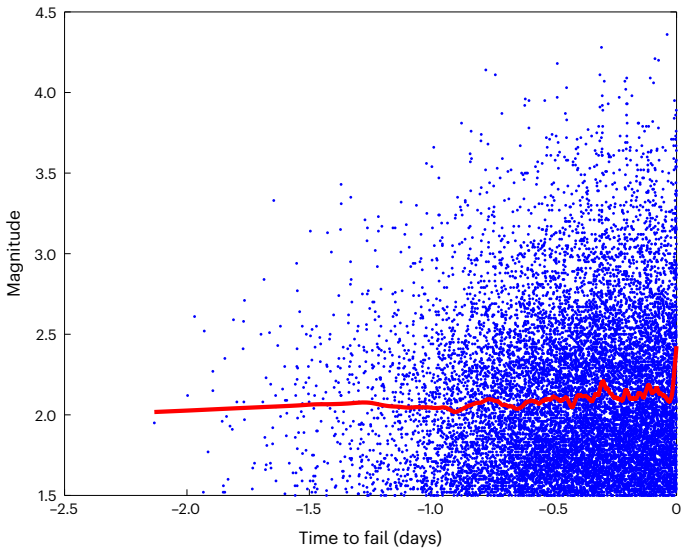

Fig. 3 | Magnitude as a function of time to mainshock. Data stacked for the last 29 cycles. The red curve represents the running mean computed by locally weighted scatterplot smoothing (LOWESS) with a span equivalent to 5% of the data.

not from properties of the ring fault. This suggests that collapse mainshocks initiate as VT events. Indeed, early parts of mainshock waveforms contain high-frequency energy comparable to VTs (Extended Data Figs. 1 and 2). If collapse mainshocks initiate as VT events, then VTs are failed mainshocks. As the average shear stress increases, ruptures are more likely to propagate farther, and the proportion of larger magnitude events increases. In this way, the likelihood of a VT 'breaking out' into a mainshock increases.

We tested this hypothesis by stacking earthquakes from the final 29 cycles aligned on subsequent mainshock times (Fig. 3), following ref. 29, and by examining (1) the frequency–magnitude distribution in the immediate pre-collapse interval relative to the background and (2) the average seismic moment rate at different times before mainshocks. VT seismicity followed a typical GR distribution with $b = 1.07$ (log daily event rate in Fig. 4a). However, for events in the 15 min before collapse, $b = 0.79$ (Fig. 4a), representing a dramatic increase in the relative number of large events in a very short interval. The standard deviation of the change in b was 0.065 ($z = 0.28/0.065 = 4.3$ with $P \ll 0.001$); thus, the change in the b-value was highly significant[31].

VT events depart from the GR line around $M \approx 3.5$, including VLP mainshocks brings the observed frequency to the GR expectation at $M \approx 4.2$. Thereafter, there is a prominent magnitude gap to $M = 5.2$. The absence of intermediate-size events combined with the large number of nearly identical events at the largest magnitude reveals a characteristic earthquake distribution[3]. The distribution is consistent with the deficit in VT events being filled in by earthquakes that 'broke out' resulting in characteristic mainshocks.

Ref. [29] reported that seismicity rates over collapse cycles follow a semi-Gaussian shape—rapidly increasing mid cycle and flattening or slightly decreasing before mainshocks, whereas cumulative seismic moment increases exponentially. We found important departures from this at shorter timescales. Magnifying the 6 h period immediately before mainshocks (Fig. 4b) revealed a dramatic increase in average seismicity and moment rate. Relative to the previous 5.75 h, the average rate in the final interval grew by 3 times (104 versus 35 events) (Methods) and moment rate by 4.75 times. We marked the onset at 15 min, although the cumulative moment rate appeared to increase quasi-exponentially during this time (Extended Data Fig. 3). The increase in the moment rate was highly significant; simulations with 100,000 randomized permutations of the catalogue failed to produce even a 2 times rate increase or 4 times moment increase in any 15 min interval in the final 6 h. Although there was cycle-to-cycle variability, 23 of the 29 cycles produced above-average rates in the final 15 min. The mean event moment in the final interval was high, but not significantly higher than the other epochs in the final 6 h. Sixteen events outside the final interval had magnitudes greater than the largest event in the final 15 min (M3.9). Thus, the late surge in moment rate was not due to a few very large events but rather to a very high rate of moderately large events (Fig. 3). The increases in earthquake rate and moment rate and the decrease in the b-value indicated that the fault entered a critical phase immediately before collapse mainshocks.

The stressing rate at the end of an average cycle was relatively low, decreasing by a factor of $e^{-T/t_c} \approx e^{-1.4/0.5} \approx 1/16$ since the previous mainshock. In an absolute sense, however, the stressing rate was very high. For a 1 MPa mainshock stress drop[17], $\dot{\tau}(T) \approx (1\,\mathrm{MPa}/0.5\ \mathrm{day})/16 \approx 40\mathrm{MPa\,yr}^{-1}$. Thus, even though the terminal 15 min interval was only 0.7% of the mean cycle duration, there was sufficient stressing to drive threshold phenomena. This resulted in a shear stress increase of ~1.3×10^{-3} MPa in the final 15 min. A nominal effective normal stress of 10 MPa (ref. 24) implies a change in spatially averaged shear to a normal stress ratio of ~1.3×10^{-4}. Thus, very modest changes in average loading resulted in dramatic changes in earthquake rupture extent. On a longer timescale, the b-value decreased as a function of relative stress (Fig. 4c), as has long been suggested[12] but difficult to demonstrate in situ.

Implications

The 4.75 times increase in the moment rate in the critical period was the product of a 1.6 times increase in the average moment and a 2.97 times increase in the rate of $M > 2.4$ earthquakes. Although the limitations of the earthquake catalogue could not rule out an increase in nucleation rate, the dramatic change in moment rate most likely arose from earthquakes getting larger, not from a higher nucleation rate.

Earthquake epicentres were non-uniformly distributed with most seismicity in the eastern sector, where the new ring fault formed in 2018 (Fig. 1a). In contrast, mainshock epicentres were concentrated in the northwestern, southeastern and southwestern sectors. This has led to the suggestion that creep was restricted to the east, with a 'seesaw' descent of the caldera block[14]. However, the inter-collapse subsidence of NPIT and CALS in the northern and southeastern sectors showed that creep was widespread[20], including where many mainshocks initiated. Multiple observations support the hypothesis that VLP mainshocks nucleated as typical VT earthquakes: (1) the largest VTs ($3.7 < M < 4.4$) tended to locate near VLP epicentres (Fig. 1a), (2) mainshocks were preceded by nearby VTs in the last 30 min of nearly all collapse cycles (Extended Data Fig. 4), (3) the relative frequency of larger magnitude VT events increased dramatically before mainshocks (Fig. 4a) and (4) the gap in the frequency–magnitude distribution (Fig. 4a) was consistent with larger VTs breaking out to form full-fault ruptures. Thus, VT and mainshock epicentral distributions were not inconsistent with the break-out hypothesis.

We suggest that extreme stress heterogeneity along new fault segments induced early nucleation of VTs at low average stress but also limited rupture extent. This is illustrated in Fig. 5, where local stresses reached static friction on the 'rough' side, but the spatially averaged driving stress τ/σ was well below the threshold for full-fault rupture (red dashed line). Along the pre-existing ring fault, where stresses were more homogeneous, rupture nucleation was delayed until the average shear stress increased. However, when local stresses reached static friction on the smoother fault, ruptures tended to extend farther with a higher probability of full-fault rupture (green dashed line in Fig. 5).

The early onset of VTs and the proximity of larger VTs and mainshock epicentres (Fig. 1a) suggest spatially variable size dependence.

https://doi.org/10.1038/s41561-023-01372-3

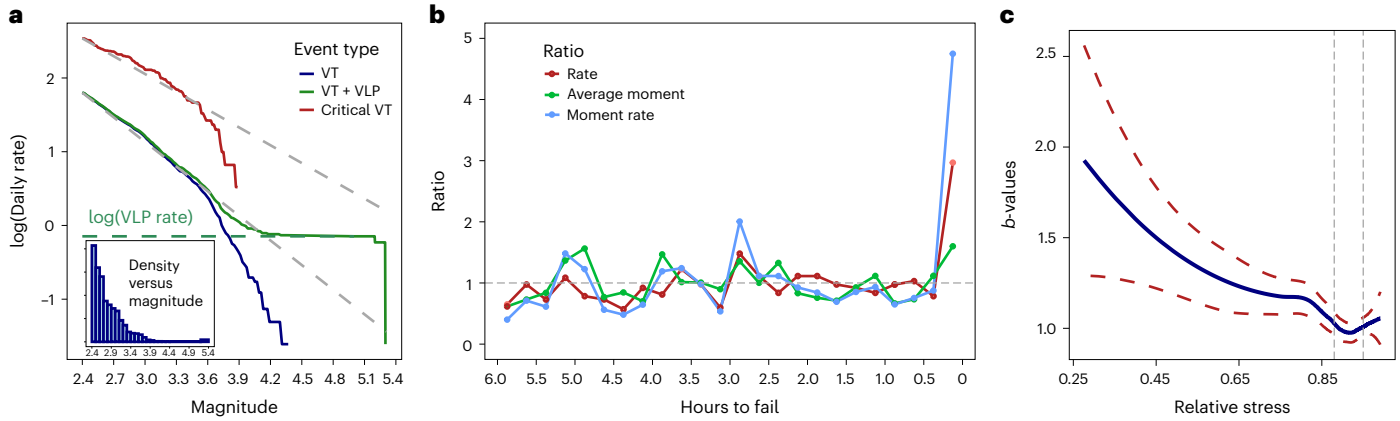

Fig. 4 | Changes in earthquake behaviour before mainshocks. a, Frequency–magnitude distribution for $M > 2.4$ events. Solid curves are $\log_{10}$ magnitude exceedance (daily) rates. Blue represents all VT events, green represents VT + VLP and red represents VT events in the critical period <15 min to mainshocks. Dashes are GR reference lines; $b = 1.07$ for all VT events, and $b = 0.79$ for events in the critical period. VLPs with $5.2 \le M \le 5.4$ bring distribution to the predicted rate at $M = 4.2$. Inset: magnitude density distribution illustrating the gap between M 4.4 and 5.2. **b**, Seismicity and moment rates in 15 min bins (plotted at bin mid-point) for the final 6 h before mainshocks. Red shows the seismicity rate, green shows the mean seismic moment and blue shows the seismic moment rate. Each point is a value normalized by the average value outside that interval. **c**, GR b-value as a function of relative stress. Red curves are 95% confidence intervals, and vertical dashed lines show the minimum and median relative stress at failure.

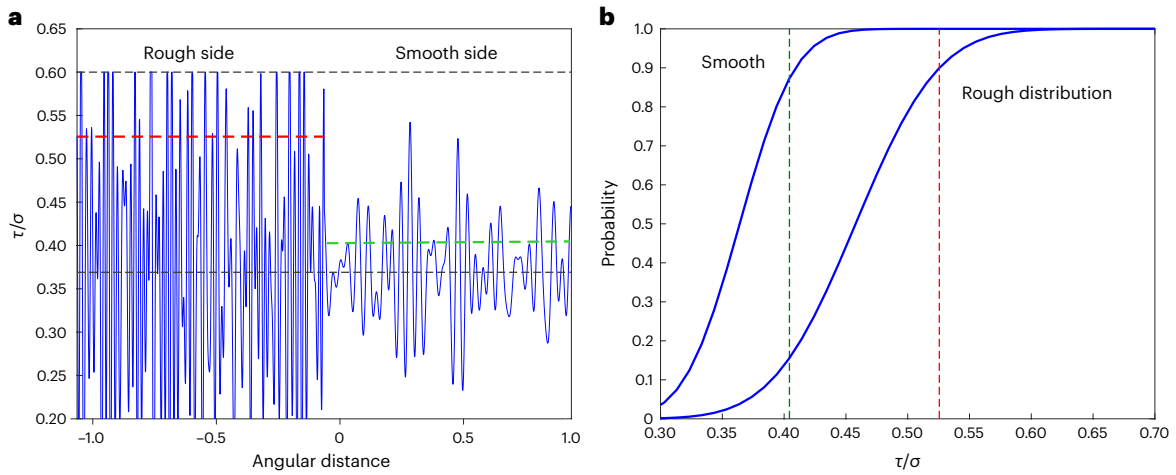

Fig. 5 | Schematic illustration of the effect of stress heterogeneity on earthquake nucleation and rupture extent. a, τ/σ as a function of angular distance, with the light dotted line indicating the mean value. The heavy dashed black line indicates static friction, whereas the red/green dashed lines show 90% probability of full-fault rupture on the 'rough'/'smooth' sides of the ring fault. **b**, Probability of full-fault rupture versus τ/σ for smooth and rough faults. Motivated by simulations of ref. 11.

Indeed, we found evidence for lower b-values in mainshock nucleation zones (Supplementary Fig. 4). Note finally that mainshocks ruptured through creeping parts of the ring fault, which strongly suggests that dynamic weakening mechanisms were activated[20].

Collapse mainshocks have notable differences from most tectonic earthquakes. The extensive ring fault creep at Kīlauea produced extreme local stressing rates, resulting in very high nucleation rates. Although rough faults with unstable frictional properties can lead to a mixture of creep and earthquake cascades[32], the extensive creep at Kīlauea required large areas of stable friction. This likely resulted from low normal stresses and/or stable ring fault frictional properties, perhaps due to hydrothermal alteration[20,33]. The absence of detectable creep before most tectonic earthquakes requires that such slip be much more limited than in the 2018 Kīlauea sequence.

Our results are consistent with a threshold phenomenon where small changes in driving stress lead to dramatic changes in the tendency for earthquakes to increase in magnitude. Heterogeneous stresses on the newly formed fault sector promoted earthquake nucleations at low average stress but inhibited large ruptures. Full-fault ruptures did not occur until the average stress reached a threshold for larger events on the smoother pre-existing fault segments.

We conclude that stress heterogeneity in general and fault geometry in particular contribute to both earthquake initiation and ultimate size. This has important implications for potentially damaging tectonic earthquakes. We do not suggest that detailed observations, such as the length of the critical phase, scale to tectonic earthquakes. Rather, we suggest that the mechanical insights gained from these data, including that rupture extent may increase dramatically with very modest changes in driving stress, carry over. Sufficiently steep break-out probability distribution functions (near the limiting case of the step functions in Fig. 5b) would lead to very few events preceding full-fault rupture. This would be consistent with mainshocks that lack detectable foreshocks, such as Parkfield 2004[34]. Future modelling studies could quantify the shape of the

schematic distributions in Fig. 5b, which would aid the interpretation of foreshock sequences.

Online content

Any methods, additional references, Nature Portfolio reporting summaries, source data, extended data, supplementary information, acknowledgements, peer review information; details of author contributions and competing interests; and statements of data and code availability are available at https://doi.org/10.1038/s41561-023-01372-3.

References

1. Reid, H. F. The elastic-rebound theory of earthquakes. *Univ. Calif. Publ. Bull. Dept. Geol.* **6**, 413–444 (1911).
2. Scholz, C. H. *The Mechanics Of Earthquakes and Faulting* (Cambridge Univ, Press, 2019).
3. Schwartz, D. P. & Coppersmith, K. J. Fault behavior and characteristic earthquakes: examples from the Wasatch and San Andreas fault zones. *J. Geophys. Res. Solid Earth* **89**, 5681–5698 (1984).
4. Weldon, R. et al. Wrightwood and the earthquake cycle: what a long recurrence record tells us about how faults work. *GSA Today* https://doi.org/10.1130/1052-5173 (2004).
5. Sawai, Y. et al. Challenges of anticipating the 2011 Tohoku earthquake and tsunami using coastal geology. *Geophys. Res. Lett.* **39**, L21309 (2012).
6. Ogata, Y., Utsu, T. & Katsura, K. Statistical features of foreshocks in comparison with other earthquake clusters. *Geophys. J. Int.* **121**, 233–254 (1995).
7. Bouchon, M., Durand, V., Marsan, D., Karabulut, H. & Schmittbuhl, J. The long precursory phase of most large interplate earthquakes. *Nat. Geosci.* **6**, 299–302 (2013).
8. Gulia, L. & Wiemer, S. Real-time discrimination of earthquake foreshocks and aftershocks. *Nature* **574**, 193–199 (2019).
9. van der Elst, N. J. B-positive: a robust estimator of aftershock magnitude distribution in transiently incomplete catalogs. *J. Geophys. Res. Solid Earth* **126**, e2020JB021,027 (2021).
10. Rivière, J., Lv, Z., Johnson, P. & Marone, C. Evolution of *b*-value during the seismic cycle: insights from laboratory experiments on simulated faults. *Earth Planet. Sci. Lett.* **482**, 407–413 (2018).
11. Fang, Z. & Dunham, E. M. Additional shear resistance from fault roughness and stress levels on geometrically complex faults. *J. Geophys. Res. Solid Earth* **118**, 3642–3654 (2013).
12. Schorlemmer, D., Wiemer, S. & Wyss, M. Variations in earthquake-size distribution across different stress regimes. *Nature* **437**, 539–542 (2005).
13. Neal, C. et al. The 2018 rift eruption and summit collapse of Kīlauea Volcano. *Science* **363**, 367–374 (2019).
14. Lai, V. H., Zhan, Z., Brissaud, Q., Sandanbata, O. & Miller, M. S. Inflation and asymmetric collapse at Kīlauea summit during the 2018 eruption from seismic and infrasound analyses. *J. Geophys. Res. Solid Earth* **126**, e2021JB022139 (2021).
15. Murray, J. & Langbein, J. Slip on the San Andreas fault at Parkfield, California over two earthquake cycles and the implications for seismic hazard. *Bull. Seismol. Soc. Am.* **96**, S283–S303 (2006).
16. Anderson, K. & Johanson, I. Incremental caldera collapse at Kīlauea Volcano recorded in ground tilt and high-rate GNSS data, with implications for collapse dynamics and the magma system. *Bull. Volcanol.* **84**, 1–26 (2022).
17. Wang, T. et al. Physics-based model reconciles caldera collapse induced static and dynamic ground motion: application to Kīlauea 2018. *Geophys. Res. Lett.* **49**, e2021GL097440 (2022).
18. Dietterich, H. R. et al. Lava effusion rate evolution and erupted volume during the 2018 Kīlauea lower east rift zone eruption. *Bull. Volcanol.* https://doi.org/10.1007/s00445-021-01443-6 (2021).
19. Anderson, K. R. et al. The 2018 eruption of Kīlauea: insights, puzzles, and opportunities for volcano science. *Annu. Rev. Earth. Planet. Sci.* https://doi.org/10.1146/annurev-earth-031621-075925 (2023).
20. Wang, T. A. et al. Ring fault creep drives volcano-tectonic seismicity during caldera collapse of Kīlauea in 2018. *Earth Planet. Sci. Lett.* **618**, 118288 (2023).
21. Fildes, R. A. et al. Interevent seismicity statistics associated with the 2018 quasiperiodic collapse events at Kīlauea, HI, USA. *Earth Space Sci.* **7**, e2019EA000766 (2020).
22. Tepp, G. Material failure and caldera collapse: insights from the 2018 Kilauea eruption. *Earth Planet. Sci. Lett.* **553**, 116621 (2021).
23. Roman, A. & Lundgren, P. Dynamics of large effusive eruptions driven by caldera collapse. *Nature* **592**, 392–396 (2021).
24. Segall, P. & Anderson, K. Repeating caldera collapse events constrain fault friction at the kilometer scale. *Proc. Natl Acad. Sci. USA* **118**, e2101469118 (2021).
25. Segall, P. et al. Caldera collapse geometry revealed by near-field GPS displacements at Kīlauea Volcano in 2018. *Geophys. Res. Lett.* **47**, e2020GL088867 (2020).
26. Kumagai, H. Very-long-period seismic signals and caldera formation at Miyake Island, Japan. *Science* **293**, 687–690 (2001).
27. Shelly, D. R. & Thelen, W. A. Anatomy of a caldera collapse: Kīlauea 2018 summit seismicity sequence in high resolution. *Geophys. Res. Lett.* **46**, 14395–14403 (2019).
28. Gibbons, S. J. & Ringdal, F. The detection of low magnitude seismic events using array-based waveform correlation. *Geophys. J. Int.* **165**, 149–166 (2006).
29. Butler, R. Volcanic earthquake foreshocks during the 2018 collapse of Kilauea Caldera. *Geophys. J. Int.* **220**, 71–78 (2020).
30. Sagy, A., Brodsky, E. E. & Axen, G. J. Evolution of fault-surface roughness with slip. *Geology* **35**, 283–286 (2007).
31. Shi, Y. & Bolt, B. A. The standard error of the magnitude-frequency b value. *Bull. Seismol. Soc. Am* **72**, 1677–1687 (1982).
32. Cattania, C. & Segall, P. Precursory slow slip and foreshocks on rough faults. *J. Geophys. Res. Solid* **126**, e2020JB020430 (2021).
33. Gailler, L. et al. 3D electrical conductivity imaging of Halema'uma'u lava lake (Kīlauea volcano). *J. Volcanol. Geotherm. Res.* **381**, 185–192 (2019).
34. Langbein, J. Preliminary report on the 28 September 2004, *M* 6.0 Parkfield, California earthquake. *Seismol. Res. Lett.* **76**, 10–26 (2005).

Methods

Average stress history

Extra-caldera displacements and tilts, which are observed to decay exponentially, are dominated by pressure changes in the shallow summit magma reservoir[24]. Given that deformation is proportional to changes in magma chamber pressure, we infer that the chamber pressure is of the form

$$p(t) = (p_0 - p_\infty)e^{-t/t_c} + p_\infty,$$

where $p_0 = p(t = 0)$ is the pressure at the onset of a cycle and $p_\infty = p(t \to \infty)$ is the asymptotic pressure that would occur in the absence of subsequent collapse. The weight of the overlying caldera block, with radius R and height L, is balanced by pressure p at its base and shear stress τ on its sides. Thus

$$\pi R^2 L\rho_c g - \pi R^2 p(t) - 2\pi RL\tau(t) = 0,$$

where ρ_c is the crustal density. Combining these equations leads to equation (1) in the main text, where $\mathcal{T} \equiv R(p_0 - p_\infty)/2L$.

Fitting t_c

The pressure decay constant t_c in each cycle was fit to data consisting of GNSS displacements measured in 5 s intervals at four extra-caldera sites (AHUP, CRIM, OUTL and PUHI) and tilt measured at 1 min intervals at a single station (SDH). The data model was a three-parameter exponential decay $y(t) = \alpha + \beta e^{-t/t_c}$. Parameters α and β are the asymptotic value and scale (amplitude), respectively. To isolate the nonlinear shape parameter of interest, t_c, we took the best fitting values $\hat{\alpha}(t_c), \hat{\beta}(t_c)$ for each t_c in a finely sampled interval and chose the value that minimized the L_1 norm of the misfits. The estimated value for observation i at site j in cycle k is $\hat{y}_{i,j,k} = \hat{\alpha}_j(t_{c,k}) + \hat{\beta}_j(t_{c,k})e^{-t_i/t_{c,k}}$. The fitted values $t_{c,k}$ minimized the objective function $g(t_{c,k}) = \sum_{i,j}|y_{i,j,k} - \hat{y}_{i,j,k}|$.

b-value estimation

b-value fits applied the Aki-Utsu maximum likelihood estimator[35]

$$\hat{b} = \frac{\log_{10}(e)}{\langle M\rangle - \left(M_c - \frac{\Delta}{2}\right)},$$

where $\langle M\rangle$ is the mean magnitude, M_c is the lower magnitude threshold, Δ is the magnitude precision and e is Euler's number, the base of the natural logarithm. For the catalogue[27], $\Delta = 0.01$ and the threshold was usually set at $M_c = 2.4$.

Seismic production rates and ratios

Catalogue event size, recorded as local magnitude, M_L, was mapped to seismic moment M_0 by $\log_{10}M_0 = 1.5M_L + 9.05$. For $M_L \le 3.0$, ref. 36 suggested $M_w = 2/3M_L + 1.0$, rather than $M_w = M_L$. However, this did not significantly alter our results (Supplementary Fig. 3). Applying power-law principles, we set the minimum magnitude cut-off M_c and calculated the excess local magnitude as $X = M_L - M_c$. The excess moment magnitude was $1.5X$. An event with excess magnitude X had moment $W(X) = 10^{1.5X}$ measured in units where $W(0) = 1$.

The seismic moment rate is the product of the event rate n/T and the average moment. Two averages are calculated:

$$\langle \text{Moment}\rangle_a = \langle 10^{1.5\mathbf{X}}\rangle = \frac{\sum 10^{(1.5X_i)}}{n}$$

$$\langle \text{Moment}\rangle_g = 10^{\langle 1.5\mathbf{X}\rangle} = 10^{1.5\bar{X}}.$$

These are, respectively, the arithmetic and geometric mean moments. Arithmetic averages are highly sensitive to rare, large 'tail events' in power-law distributions. Geometric averages often better represent 'typical' size. For these data, $M > 2.4$ events had an arithmetic average moment of 11.73 and a geometric average of 3.90. The median moment was 2.63.

Let B denote a catalogue subset with time duration T and n events at excess magnitudes $\mathbf{X} = (X_1, X_2, \ldots, X_n)$. The total moment production rate in B, μ, is the event rate, n/T times the average moment:

$$\mu(\text{B}) = \frac{n(\text{B})}{T(\text{B})}\langle \text{Moment(B)}\rangle.$$

The catalogue subsets A and B are comparable in terms of the production ratio: $\rho[\text{A/B}] = \mu[\text{A}]/\mu[\text{B}]$.

Data availability

GNSS data are available from the UNAVCO archive (https://www.unavco.org/data/data.html). Seismic data are from the USGS HVO (https://doi.org/10.7914/SN/HV). Data can be accessed at http://ds.iris.edu/mda/HV. Any use of trade, firm or product names is for descriptive purposes only and does not imply endorsement by the US Government.

References

35. Marzocchi, W. & Sandri, L. A review and new insights on the estimation of the b-value and its uncertainty. *Ann. Geophys.* **46**, 1271–1282 (2003).
36. Deichmann, N. Theoretical basis for the observed break in M_L/M_w scaling between small and large earthquakes. *Bull. Seismol. Soc. Am.* **107**, 505–520 (2017).

Acknowledgements

We thank B. Ellsworth for helpful discussions, A. Flinders and N. Van Der Elst of the USGS for internal reviews and W. Marzocchi for improving the manuscript. This study was supported by the National Science Foundation EAR-2040425 (P.S.).

Author contributions

P.S.: conceptualization, methodology, writing—original draft, supervision. M.V.M.: data analysis, statistical computations, modelling and interpretation, contributions to writing and editing. D.R.S.: earthquake location and catalogue analysis, editing. T.A.W.: analyses of time/spectral-domain comparisons between VT and VLP events, editing. K.R.A.: analysis of geodetic data, editing.

Competing interests

The authors declare no competing interests.

Additional information

Extended data is available for this paper at https://doi.org/10.1038/s41561-023-01372-3.

Supplementary information The online version contains supplementary material available at https://doi.org/10.1038/s41561-023-01372-3.

Correspondence and requests for materials should be addressed to Paul Segall.

Peer review information *Nature Geoscience* thanks the anonymous reviewers for their contribution to the peer review of this work.

https://doi.org/10.1038/s41561-023-01372-3

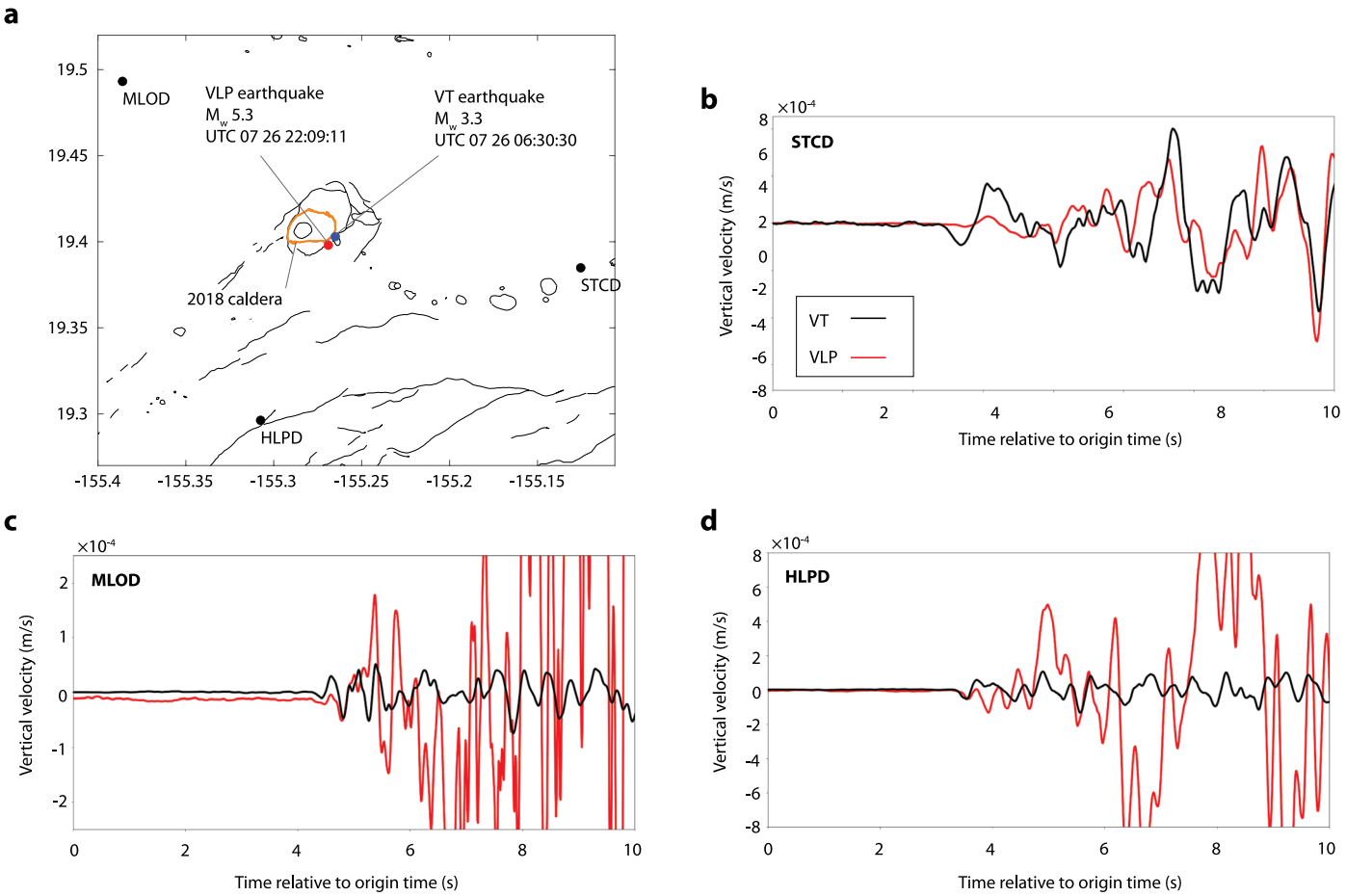

Extended Data Fig. 1 | Comparison of velocity waveforms from closely located VT and VLP earthquakes. a, map view of Kīlauea summit, with VT and VLP epicenters, as well as three broadband stations. **b**,**c**,**d**, first 10 seconds of vertical velocity seismograms at stations STCD, MLOD, HLPD. VLP time shifted to match VT.

https://doi.org/10.1038/s41561-023-01372-3

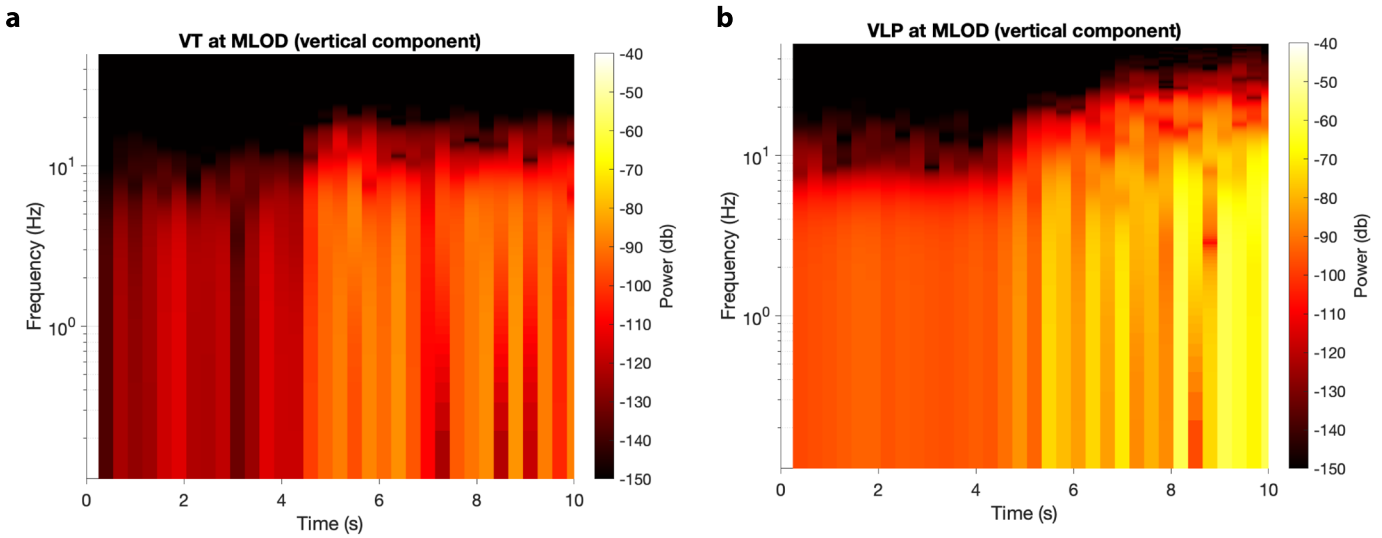

Extended Data Fig. 2 | Comparison of closely located VT and VLP vertical component spectrograms at station MLOD. a, VT **b**, VLP.

https://doi.org/10.1038/s41561-023-01372-3

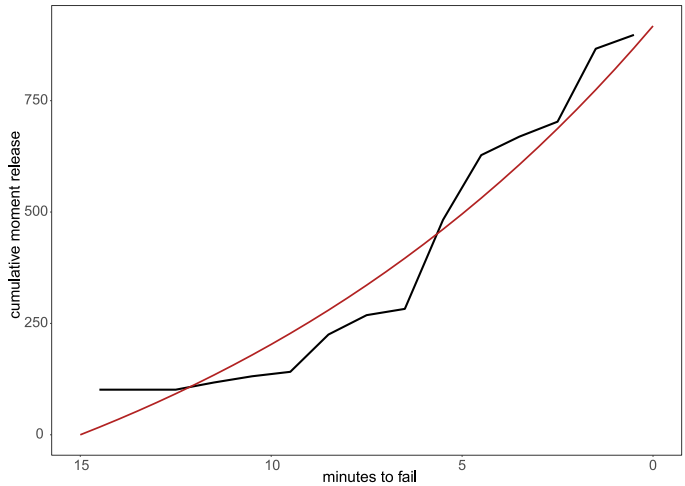

Extended Data Fig. 3 | Cumulative seismic moment in the final 15 minute stacked catalog. Moments are multiples of the moment of an $M = 2.4$ event, which is 4.47×10^{12} Nm. Red line shows exponential fit.

https://doi.org/10.1038/s41561-023-01372-3

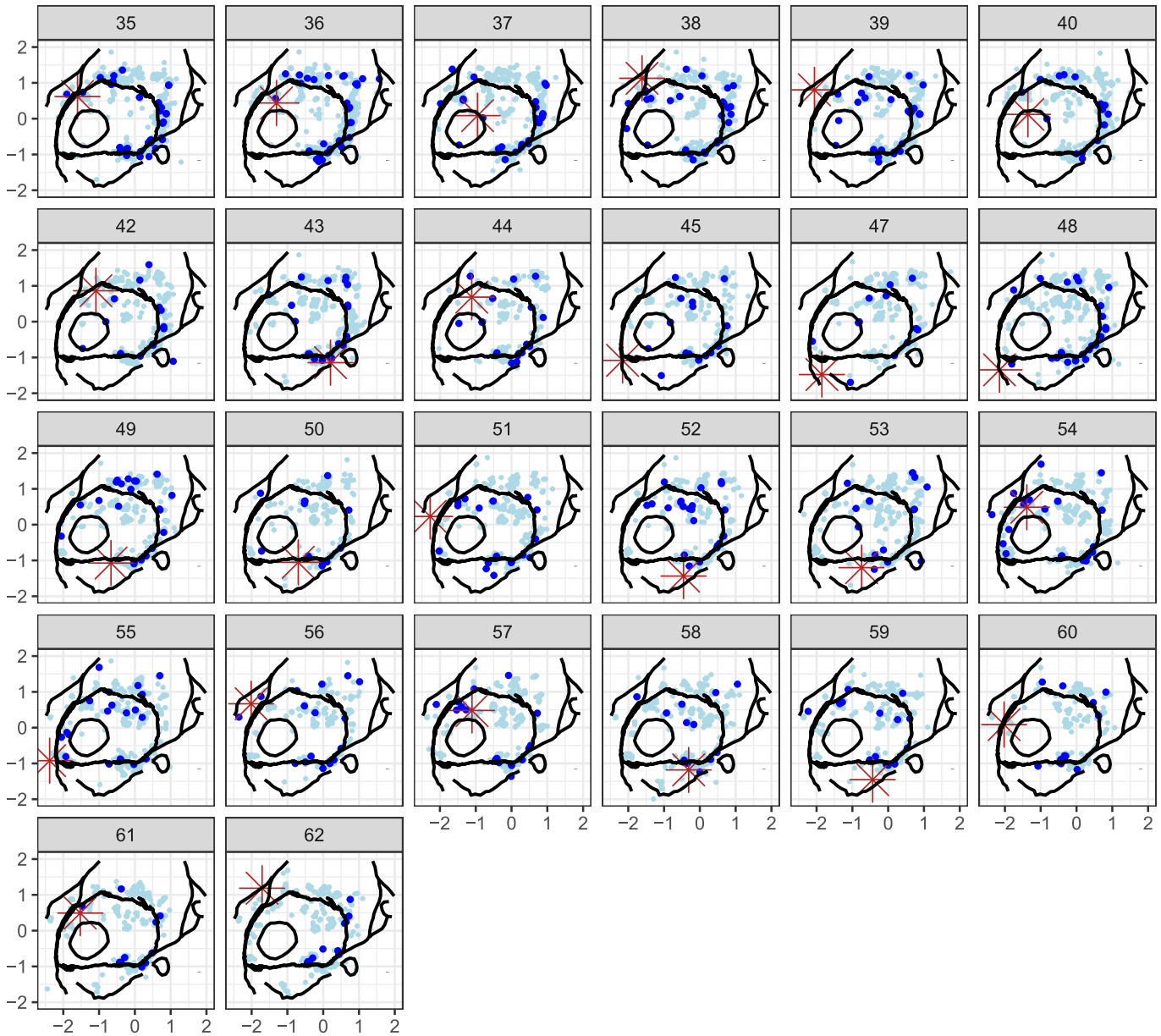

Extended Data Fig. 4 | Mainshock epicentral regions are active in the 30 minutes prior to mainshocks. Epicenters of earthquakes in 26 of the last 29 collapse cycles. (26 depicted VLP locations are from Shelly and Thelen (2019). Three VLPs locations, in Cycles 34, 41, and 46, are not available in the Shelley-Thelen catalog.) Epicenters colored by time to collapse. Light blue: background time to failure > 30 minutes, dark blue: last 30 minutes; red stars mainshocks epicenters. Note that nearly all mainshocks are preceded by nearby VT events in the final 30 minutes, supporting the hypothesis that mainshocks are runaway VT earthquakes.